Initial response mechanism and local contact stiffness analysis of the Floating Two-stage Buffer Collision-prevention System under ship colliding

Kai Lu[1], Xu-Jun Chen[1,2,*], Zhen Gao[2], Liang-Yu Cheng[1] and Guang-Huai Wu[3]

[1] College of Field Engineering, Army Engineering University of PLA, Nanjing 210007, China; lukai_30@sina.com(K.L.); clychmy@qq.com(L.-Y.C.)

[2] Department of Marine Technology, Norwegian University of Science and Technology, Trondheim 7491, Norway; zhen.gao@ntnu.no

[3] Nanjing Guangbo Engineering Technology Co.LTD，Nanjing 210046, China; wuguanghuai@sina.com

* Correspondence: chenxujun213@sina.com

Abstract: A Floating Two-stage Buffer Collision-Prevention System (FTBCPS) has been proposed to reduce the impact loads on the bridge pier in this paper. The anti-collision process can be mainly divided into two stages. First, reduce the ship velocity and change the ship initial moving direction with the stretching and fracture of the polyester ropes. Second, consume the ship kinetic energy with the huge damage and deformation of the FTBCPS and the ship. The main feature of the FTBCPS lies in the first stage and most of the ship kinetic energy can be dissipated before the ship directly impacts on the bridge pier. The contact stiffness value between the ship and the FTBCPS can be a significant factor in the first stage and the calculation method of it is the focus of this paper. The contact force, the internal force and the general equation of motion have been given in the first part. The structure model of the ship and the FTBCPS are then established in the ANSYS Workbench. After that, 38 typical load cases of the ship impacting on the FTBCPS are conducted in LS-DYNA. The reduction processes of the ship kinetic energy and the ship velocity in different load cases have been investigated. It can be summarized that the impact angle and the ship initial velocity are the main factors in the energy and velocity dissipation process. Moreover, the local impact force-depth curves have also been studied and the impact angle is found to be the only significant factor on the ship impact process. Next, the impact force-depth curves with different impact angles are fitted and the contact stiffness values are accordingly calculated. Finally, the impact depth range, the validity of the local simulation results and the consistency of the fitted stiffness value are verified respectively, demonstrating that the fitted stiffness values are applicable in the global analysis.

Key words: Offshore structures; Floating Two-stage Buffer Collision-prevention System; dynamics principle; initial response mechanism; contact stiffness values

1. Introduction

Bridge piers in rivers or sea are under a potential threat of the ship collision accidents in the navigable waters and the anti-collision devices are established to reduce the damages to piers and bridges. A bunch of empirical formulas (Minorsky 1958) are given to estimate the ship-pier loads based on the parameters, e.g. the ship size, the ship displacement and the ship velocity, but most of them can

be only applicable to the ship-ship collisions or the ship-offshore structure collisions.

The general design of bridge piers focuses on the permanent load and the live load in the vertical direction, but the attention paid to horizontal loads is insufficient. Thus, the anti-collision structures are indispensable and the structural responses of bridge piers under ship impacts are referential to their design. Consolazio and Davidson (2008) proposed an algorithm to simplify the additional force on the ship forward and the results of it are validated by full-scale experiments. The dynamic vessel collision analysis techniques (Consolazio et al. 2009) are developed with mass-related components of bridge response and alternative barge bow stiffness with the crush curves. Gholipour et al. (2019a; 2019b) assessed the failure modes of the piers with the correlation analyses method. Guo et al. (2020a; 2020b) found the peak displacement of pier and local deformation in the piles significantly increases as scour depth increases.

The collision cases between ships and bridges (Moe et al. 2017a; Moe et al. 2017b; Kameshwar and Padgett 2018; Wang and Morgenthal 2017; Wang and Morgenthal 2018a; Chen et al. 2019) are studied in many articles in recent years, but the studies on the collision cases between ships and anti-collision structures are not common. An innovative foam-filled lattice composite bumper system (Zhu et al. 2018) shows the properties of good energy absorbing and highly designable and performs an obvious advantage in the peak impact force and duration. Sha et al. (2019a) present a numerical investigation of ship collision response for a floating pontoon. The bridge girder design against ship forecastle collision loads (Sha et al. 2019b) was also discussed and a simple but effective strengthening method was proposed to increase the collision resistance of steel bridge girders. A floating steel fender system for bridge pier protection (Jiang and Chorzepa 2016) was introduced and the performance of it had been evaluated with an explicit dynamic finite-element analysis code. The introduced fender system noticeably reduced the peak impact force on pier and on the colliding vessel while extending the impact duration simultaneously. Fan et al. (2020) developed a general analytical procedure to estimate the force-deformation relationship of steel fenders under various bow impacts rapidly. The deformation mechanisms and models as well as the primary individual members of steel fenders during various collision scenarios were discussed in detail and the approach developed could be capable of predicting the crush depth and peak impact force of a steel fender with good accuracy. A novel steel-PAFRC (Preplaced Aggregate Fibre Reinforced Concrete) composite fender for bridge pier protection (Manohar et al. 2020) was an innovative composite fender structure consisting of corrugated steel and PAFRC, which was tested through a drop weight impact test. Corrugated plates of steel are intended to absorb energy and stiff guard outer panels made with PAFRC exhibit enhanced resistance to impact and ductility. A novel crashworthy device (Wang and Morgenthal 2018b) was developed, which is comprised of vertically supported impact cap connected to the bridge pier using a series of steel beams

in a frame-type arrangement. The sacrificial steel structure is designed to form plastic hinges for energy dissipation whilst limiting the force transmitted to the protected pier. The strategy (Wang et al. 2020) of using reduced cross-sections for certain steel beams in the device is proposed to limit plastic mechanisms within certain structural components whilst ensuring that others remain elastic during impact and it would greatly facilitate the restoration process of such devices after an impact event by replacing only those structural components where plastic deformations have occurred.

A Floating Two-stage Buffer Collision-Prevention System (FTBCPS) is composed of a floater, connecting lines, polyester ropes, anchors, and anchor chains, as shown in Figure 1. The damping cables are made up of a series of polyester ropes with a large elongation. The connecting lines can be the rigid chains made up of high strength steels. Damping cables are mounted on the floater, part of them connected to the bridge pier by the connecting lines and the others are connected to the anchor chains. When the floater goes advance under the ship impact, the ship kinetic energy will be consumed by the breaking of polyester ropes. The energy dissipation can be mainly divided into two stages. First, the floater suffers an increasing tension load from the connecting lines and the damping cables when it starts moving from the rest under the ship impact. The polyester rope breaks once the tension load acting on it exceeds its bearing capacity, at the same time, more and more polyester ropes will be stressed with the floater's movement. Polyester ropes also provide the reaction forces on the floater. This stage will last a long duration for the large number of polyester ropes in the anti-collision system. Then, if all the damping cables become invalid and the floater keeps moving until touching the bridge pier, the floater will undergo a large partial deformation and consume the ship kinetic energy directly. The local impact in the first stage consumes part of the ship kinetic energy and influences the global response of the ship, which cannot be ignored. To emphasize an important point, the force transferred from the connecting lines to the pier must not exceed the horizontal bearing capacity of pier, which means that FTBCPS can prolong the force duration of the bridge pier and reduce the peak force. In addition, the FTBCPS can also protect bridge piers by changing the ship original movement direction. The whole impact process can be decomposed into multiple stages of contact and separation, and the entire impact process can hardly be conducted with a coupled collision analysis with FEA directly. If only the structural analysis software is introduced to the collision simulation, the structural response of the contact part will be studied, but the dynamic response of the ship and the floater will be difficult to be evaluated. A comprehensive analysis method (Sha et al. 2017) can be used to study the global response and the local response of the FTBCPS under the ship impact and the whole process can be converted into a two-step analysis. The local analysis is conducted first to find out the relationship between the ship-floater impact force and the impact depth, and the database of the contact stiffness values can be established according to it. Then the global analysis is conducted to study the dynamic

response of the ship and the floater with the real-time call of the database. The anti-collision effect of the current FTBCPS design can be evaluated by the two-step analysis, and a further detailed design can be carried out based on it.

The statuses of the ship and the floater, e.g. relative position, relative velocity, relative rotation angle, will be constantly changing at the initial stage in the global analysis. However, no matter how the statuses of the two change, the contact force can always be solved based on the collision surface of the floater. That is, the normal contact force can be related to the impact depth, and the tangential force can be obtained by the method of multiplying the normal force with a reasonable sliding friction coefficient. Therefore, it is important to explore the relationship between the normal force and the impact depth in local analysis and that is the focus of this article.

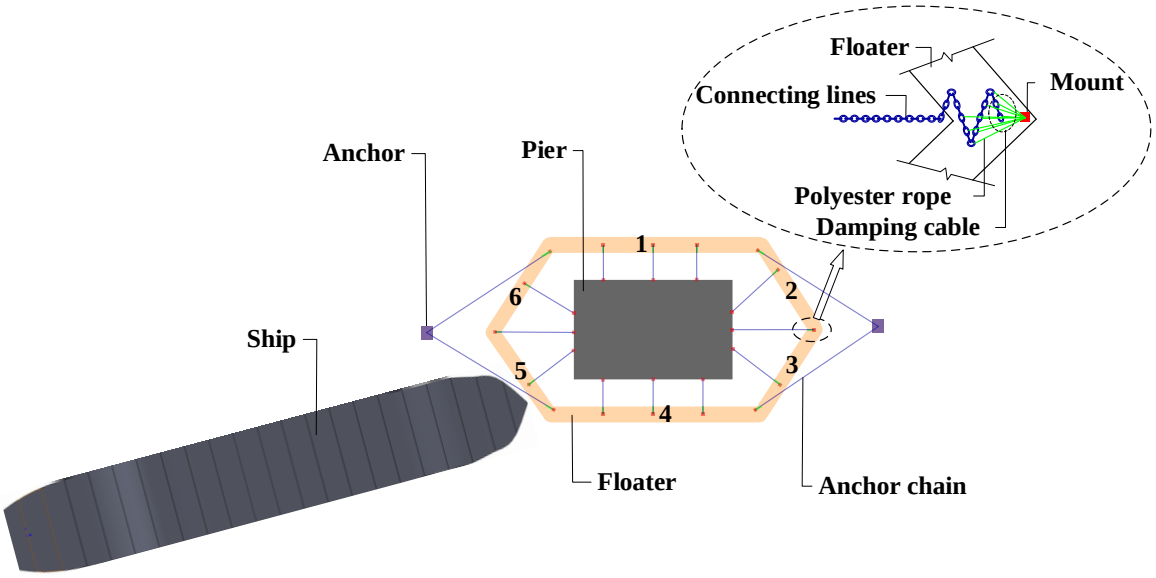

Figure 1. The schematic layout of the FTBCPS arrangement.

2. Computational dynamics theory

2.1 Assumptions and the general equation for the local analysis

The assumptions in local analysis are set below.

(1) The surfaces close to the pier in beam 1~4 of the floater will be set fixed to the ground in the inside. The local ship collision problem can be simplified into a structural collision model between the ship and the floater. According to Figure 1, the positions connected to the connecting lines on the beam 1~4 will suffer tensile force when the beam 5 is hit by the ship. The freedom of the corresponding positions on beam 1~4 will be limited for an easier and better study on the deformation of the ship and the floater, which conforms to the actual condition of the floater.

(2) The added water mass coefficient of the ship can be set 0.2 tentatively. According to the model

test results and the hydrodynamic analysis (Petersen 1982) and the verification results by Wang et al. (2002), it is reasonable to set added mass coefficient to 0.2.

(3) The ship will have an initial velocity in the normal direction of the contact surface, and only the horizontal motion of the ship will be allowed. The tangential contact force can be gained from the normal contact force and the friction factor in the global analysis. Thus, the normal contact force will be focused on the local analysis.

The ship and floater are modeled with shell finite elements and the collision problem is essentially converted into a contact problem of the planar shell elements. The contact process is associated with time and accompanied with the evolution of material nonlinearity and geometric nonlinearity. The contact region, the geometry and the dynamic state of the contact surface are all unknown in advance. The time increment method can be used to calculate the kinetic parameters at the subsequent moment with the known parameters at this moment, so it is chosen to deal with the contact problem here. Then the general equation of the local simulation is given as below.

$$\boldsymbol{M}\left(\mathrm{d}^2\boldsymbol{u}^{t+\Delta t}/\mathrm{d}t^2\right)+\left(\boldsymbol{K}_L^t+\boldsymbol{K}_{NL}^t\right)\boldsymbol{u}^{t+\Delta t}-\boldsymbol{Q}_c^{t+\Delta t}=\boldsymbol{Q}_L^{t+\Delta t}-\boldsymbol{F}^{t+\Delta t} \tag{1}$$

where $\boldsymbol{u}^{t+\Delta t}$ and $\mathrm{d}^2(\boldsymbol{u}^{t+\Delta t})/\mathrm{d}t^2$ refer to the displacement vector and the acceleration vector at the time increment step $t+\Delta t$. $\boldsymbol{K}_L^t$ and $\boldsymbol{K}_{NL}^t$ are the stiffness matrices corresponding to the linear strain and nonlinear strain of the shell element at the time increment step t. $\boldsymbol{F}^{t+\Delta t}$ refers to the internal force of the shell element at the time increment step t. $\boldsymbol{Q}_c^{t+\Delta t}$ and $\boldsymbol{Q}_L^{t+\Delta t}$ refer to the equivalent node contact force and external nodal load at the time increment step $t+\Delta t$.

The contact process is complex and involves structural nonlinearity and material nonlinearity, thus it is necessary to consider both the stiffnesses of linear and nonlinear. $\boldsymbol{K}_L^t$ is gained from the constitutive relation of the material and $\boldsymbol{K}_{NL}^t$ is related to the second Piola-Kirchhoff stress tensor. They can be integrated into the general equation to describe the relationship between the contact force and structural deformation during contact process. Then we will focus on the theories on contact node pairs detecting, contact force, internal force, and the time-domain integration methods (Wang 2003) to solve the general equations of motions.

2.2 Contact force

In the numerical simulations, the contact process can be replaced by the contact of the slave nodes defined on the contact surface and the master nodes defined on the target surface. Impenetrability means the objects are not allowed to penetrate (invade or cover) each other and it is an important principle in the contact process. Therefore, the relationship between surfaces can be divided into three typical types: separation, adhesion and sliding. The contact node pairs exist in the relationship of adhesion and sliding. The relationship of adhesion refers to the contact state without relative sliding

and the relationship of sliding refers to the contact state with relative sliding. The first step of the time increment method is to detect contact node pairs and the trial-check iterative method is adopted. The trial-check iterative method contains two parts: first is to make a hypothesis of the contact area in the first iteration of this step according to the results of the previous step and the load conditions set in this step, second is to check the hypothesis proposed. The equality constraint means the constraint with an equal sign and the inequality constraint means the constraint with the inequal sign. The check requirements are a series of inequality constraint. If the inequality constraints in kinematics or dynamics listed in Table 1 are true, they will be converted into the equality constraint according to the hypothesis. The equality constraint reached will be served as the definite solution requirements in the calculation of the contact force. Then any point on the contact surface will be detected with the check requirements, and the solutions of this step will be carried out and the next time increment step will be taken if no points violate the check requirements. On the contrary, another hypothesis, search and iteration will be made until all points on the contact surface meet the check requirements.

Table 1. Definite solution requirements and check requirements.

Contact state		Definite solution requirements	Check requirements
Contact	Adhesion	(1) $u_{\mathrm{A,N}}-u_{\mathrm{B,N}}+\bar{g}_{\mathrm{N}}^{t}=0$ (2) $\boldsymbol{u}_{\mathrm{A,T}}-\boldsymbol{u}_{\mathrm{B,T}}=\boldsymbol{0}$	(1) $F_{\mathrm{A,N}}^{t+\Delta t}>0$ Convert into separation if dissatisfaction (2) $\left\|\boldsymbol{F}_{\mathrm{A,T}}^{t+\Delta t}\right\|-\mu\left\|\boldsymbol{F}_{\mathrm{A,N}}^{t+\Delta t}\right\|<0$ Convert into sliding if dissatisfaction
	Sliding	(1) $u_{\mathrm{A,N}}-u_{\mathrm{B,N}}+\bar{g}_{\mathrm{N}}^{t}=0$ (2) $\left\|\boldsymbol{F}_{\mathrm{A,T}}^{t+\Delta t}\right\|-\mu\left\|\boldsymbol{F}_{\mathrm{A,N}}^{t+\Delta t}\right\|=0$	(1) $F_{\mathrm{A,N}}^{t+\Delta t}>0$ Convert into separation if dissatisfaction (2) $\left(\boldsymbol{u}_{\mathrm{A,T}}-\boldsymbol{u}_{\mathrm{B,T}}\right)\cdot\boldsymbol{F}_{\mathrm{A,T}}^{t+\Delta t}<0$ & $\left\|\boldsymbol{u}_{\mathrm{A,T}}-\boldsymbol{u}_{\mathrm{B,T}}\right\|>\varepsilon_s$ Convert into sliding if dissatisfaction Search for new contact node pairs if satisfaction
Separation		$\boldsymbol{F}_{\mathrm{A}}^{t+\Delta t}=\boldsymbol{F}_{\mathrm{B}}^{t+\Delta t}=\boldsymbol{0}$	$\left(\boldsymbol{x}_{\mathrm{A}}^{t+\Delta t}-\boldsymbol{x}_{\mathrm{B}}^{t+\Delta t}\right)\cdot\boldsymbol{n}_{\mathrm{B}}^{t+\Delta t}>\varepsilon_d$ Convert into adhesion if dissatisfaction

where the subscript A and B refer to the parameters in local coordinates of the contact surface A and the target surface B. $u_{\mathrm{A,N}}$ and $u_{\mathrm{B,N}}$ refer to the normal displacements of the slave node and the master node. $\bar{g}_{\mathrm{N}}^{t}$ refers to the distance of the slave node and the master node in the direction of $\boldsymbol{n}_{\mathrm{B}}^{t+\Delta t}$. $\boldsymbol{u}_{\mathrm{A,T}}$ and $\boldsymbol{u}_{\mathrm{B,T}}$ refer to the tangential displacement vectors of the slave node and the master node in the time interval between t and $t+\Delta t$. $\boldsymbol{F}_{\mathrm{A,N}}^{t+\Delta t}$ and $\boldsymbol{F}_{\mathrm{A,T}}^{t+\Delta t}$ refer to the normal contact force and the tangential contact force between the contact surface and the target surface.

When the definite solution requirements are introduced to the penalty function as an additional functional in the variational principle, the equivalent nodal force between the kth contact pair can be expressed as

$$\left(\boldsymbol{Q}_c^{t+\Delta t}\right)_k = -\left(\boldsymbol{N}_c^T \boldsymbol{\theta}^{t+\Delta t} \boldsymbol{F}_{\mathrm{A}}^{t+\Delta t}\right)_k \tag{2}$$

$$\boldsymbol{N}_c = \begin{bmatrix} \boldsymbol{I} & -\boldsymbol{N}_1 & -\boldsymbol{N}_2 & -\boldsymbol{N}_3 & -\boldsymbol{N}_4 \end{bmatrix}$$

$$\boldsymbol{I} = \boldsymbol{I}_{3*3} \qquad \boldsymbol{N}_i = \boldsymbol{I} N_i \qquad (i = 1,2,3,4)$$

$$\boldsymbol{\theta} = \begin{bmatrix} \boldsymbol{e}_1 & \boldsymbol{e}_2 & \boldsymbol{e}_3 \end{bmatrix} = \begin{bmatrix} e_{1x} & e_{2x} & e_{3x} \\ e_{1y} & e_{2y} & e_{3y} \\ e_{1z} & e_{2y} & e_{3z} \end{bmatrix}$$

where $N_1 \sim N_4$ refer to the interpolation functions of the shell element nodes. $\boldsymbol{\theta}$ refers to the coordinate transformation matrix. e_{Ji} ($J = 1,2,3, i = x, y, z$) refers to the direction component of the x, y and z direction in the global coordinate system.

Moreover, the contact force can be expressed as

$$F_{\mathrm{A,N}}^{t+\Delta t} = -F_{\mathrm{B,N}}^{t+\Delta t} = -\alpha\left(u_{\mathrm{A,N}} - u_{\mathrm{B,N}} + \bar{g}_{\mathrm{N}}^t\right) = -\alpha \bar{g}_{\mathrm{N}}^{t+\Delta t} \tag{3}$$

$$F_{\mathrm{A},J}^{t+\Delta t} = -F_{\mathrm{B},J}^{t+\Delta t} = -\alpha\left(u_{\mathrm{A},J} - u_{\mathrm{B},J}\right) \qquad J = 1,2 \tag{4}$$

where J refers to the two tangent directions of the contact surface. $\boldsymbol{\alpha}$ refers to the penalty factor which is used to express the relationship of the contact force and relative displacement of the two contact surfaces.

Then convert Eqs.(3) and (4) into the matrix form as

$$\boldsymbol{F}_{\mathrm{A}}^{t+\Delta t} = -\boldsymbol{\alpha}_{st}\left(\boldsymbol{u}_{\mathrm{A}} - \boldsymbol{u}_{\mathrm{B}}\right) - \alpha \bar{\boldsymbol{g}}^t \tag{5}$$

$$\boldsymbol{\alpha}_{st} = \begin{bmatrix} \alpha & & \\ & \alpha & \\ & & \alpha \end{bmatrix} \qquad \bar{\boldsymbol{g}}^t = \begin{bmatrix} 0 \\ 0 \\ \bar{g}_{\mathrm{N}}^t \end{bmatrix}$$

The slave node n_s can establish the contact relationship with the closest master node m_s, just as shown in Figure 2. $\boldsymbol{c}_i$ and $\boldsymbol{c}_{i+1}$ indicate two boundary vectors from node m_s. $\boldsymbol{s}$ indicates the vector from master node to slave node and $\boldsymbol{g}$ indicates the vector from the master node to the candidate slave node (Li and Mao 2014). The master node can be determined by Eq.(6) in general. However, there may be more than one face element that satisfies Eq.(6) along with the process of the slave node moving towards the target face. Then Eq.(7) can be used to select the node which makes the smallest angle between $\boldsymbol{g}$ and $\boldsymbol{c}_j$ as the master node.

$$\begin{cases}(\boldsymbol{c}_i \times \boldsymbol{s})\cdot(\boldsymbol{c}_i \times \boldsymbol{c}_{i+1}) > 0 \\ (\boldsymbol{c}_i \times \boldsymbol{s})\cdot(\boldsymbol{s} \times \boldsymbol{c}_{i+1}) > 0\end{cases} \tag{6}$$

$$\max\left(\frac{\mathbf{g}\cdot\mathbf{c}_j}{|\mathbf{c}_j|} \quad j = 1,2,3,4,\ldots\right) \tag{7}$$

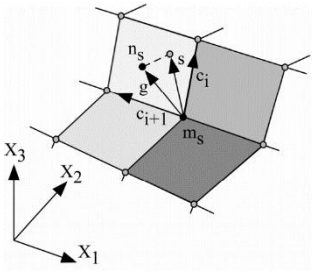

Figure 2. Search process of the master node.

The contact node pair of node P and node Q can be determined by the search process above. The relative displacement of the two nodes can be expressed as

$$\boldsymbol{u}_{(\mathrm{P})} - \boldsymbol{u}_{(\mathrm{Q})} = \boldsymbol{N}_c \boldsymbol{u}_c \tag{8}$$

$$\boldsymbol{u}_c = \left[\boldsymbol{u}_{(\mathrm{P})}^{\mathrm{T}} \quad \boldsymbol{u}_{(1)}^{\mathrm{T}} \quad \boldsymbol{u}_{(2)}^{\mathrm{T}} \quad \boldsymbol{u}_{(3)}^{\mathrm{T}} \quad \boldsymbol{u}_{(4)}^{\mathrm{T}}\right]^{\mathrm{T}}$$

where $\boldsymbol{u}_{(\mathrm{P})}$ and $\boldsymbol{u}_{(\mathrm{Q})}$ refer to the displacement of the node P and node Q. $\boldsymbol{u}_{(1)}$ ~ $\boldsymbol{u}_{(4)}$ refer to the node displacements of the 4-node shell element.

Convert Eq.(8) into the local coordinate system.

$$\boldsymbol{u}_{\mathrm{A}} - \boldsymbol{u}_{\mathrm{B}} = \left(\boldsymbol{\theta}^{t+\Delta t}\right)^{\mathrm{T}} \boldsymbol{N}_c \boldsymbol{u}_c \tag{9}$$

Substitute Eq.(9) into Eq.(5) and the contact force is further expressed as

$$\boldsymbol{F}_{\mathrm{A}}^{t+\Delta t} = -\boldsymbol{\alpha}_{st}\left(\boldsymbol{\theta}^{t+\Delta t}\right)^{\mathrm{T}} \boldsymbol{N}_c \boldsymbol{u}_c - \alpha \bar{\boldsymbol{g}}^t \tag{10}$$

Substitute Eq.(10) into Eq.(2) and the equivalent nodal force between the kth contact pair is further expressed as

$$\left(\boldsymbol{Q}_c^{t+\Delta t}\right)_k = -\left(\alpha \boldsymbol{N}_c^T \boldsymbol{N}_c \boldsymbol{u}_c + \alpha \bar{g}_{\mathrm{N}}^t \boldsymbol{N}_c^T \boldsymbol{e}_3^{t+\Delta t}\right)_k \tag{11}$$

The equivalent node contact force $\mathbf{Q}_c^{t+\Delta t}$ can be gained by the superposition of $(\boldsymbol{Q}_c)_k$.

$$\boldsymbol{Q}_c^{t+\Delta t} = \sum_{k=1}^{n_c}\left(\boldsymbol{Q}_c^{t+\Delta t}\right)_k \tag{12}$$

2.3 Internal force

The evolution history of the stress and strain during loading can be obtained by the time increment

method to ensure the accuracy and the stability of the solution under large deformation conditions. The virtual work of the external load $W^{t+\Delta t}$ can be obtained based on the principle of virtual displacement at the time increment step $t+\Delta t$.

$$W^{t+\Delta t}=\int_{t_V} S_{ij}^{t}\delta^{t}\varepsilon_{ij}^{t}\mathrm{d}V+\int_{t_V}\tau_{ij}^{t}\delta^{t}\eta_{ij}^{t}\mathrm{d}V+\int_{t_V}\tau_{ij}^{t}\delta^{t}e_{ij}^{t}\mathrm{d}V \tag{13}$$

where the subscript t_V refers to the integral range is all the planar shell elements in the ship and floater. S_{ij}^{t}, τ_{ij}^{t} and ε_{ij}^{t} refer to the Kirchhoff stress tensor, Cauchy stress tensor and Green strain tensor. e_{ij}^{t} refers to the linear term of the Green strain tensor ε_{ij}^{t} on the increment u_i and η_{ij}^{t} refers to the quadratic term of Green strain tensor ε_{ij}^{t} on the increment u_i. δ refers to the variation of the infinitesimal strain of each parameter.

Eq.(13) can be further rewritten in the dynamic analysis as the below.

$$\boldsymbol{M}\left(\mathrm{d}^2(\boldsymbol{u}^{t+\Delta t})/\mathrm{d}t^2\right)+\left(\boldsymbol{K}_L^{t}+\boldsymbol{K}_{NL}^{t}\right)\boldsymbol{u}=\boldsymbol{Q}^{t+\Delta t}-\boldsymbol{F}^{t} \tag{14}$$

$$\boldsymbol{K}_L^{t}=\sum\int_{t_V}\left(\boldsymbol{B}_L^{t}\right)^{\mathrm{T}}\boldsymbol{D}^{t}\boldsymbol{B}_L^{t}\mathrm{d}V \tag{15}$$

$$\boldsymbol{K}_{NL}^{t}=\sum\int_{t_V}\left(\boldsymbol{B}_{NL}^{t}\right)^{\mathrm{T}}\boldsymbol{\tau}^{t}\boldsymbol{B}_{NL}^{t}\mathrm{d}V \tag{16}$$

$$\boldsymbol{F}^{t}=\sum\int_{t_V}\left(\boldsymbol{B}_L^{t}\right)^{\mathrm{T}}\hat{\boldsymbol{\tau}}^{t}\mathrm{d}V \tag{17}$$

where $\boldsymbol{B}_L^{t}$ and $\boldsymbol{B}_{NL}^{t}$ refer to the transformation matrix of linear strain and nonlinear strain. $\boldsymbol{D}^{t}$ refers to the material constitutive matrix. $\boldsymbol{\tau}^{t}$ and $\hat{\boldsymbol{\tau}}^{t}$ refer to the Cauchy stress matrix and array.

Based on the maximum strain theory, the value of the failure strain can be set in advance and all the parameters in the strain matrix would be checked after each time increment step. The element will be designated as failed and eliminated in the next time increment step if the failure strain is exceeded.

2.4 Time-domain integration methods for solving the general equation

When the explicit method introduced to the contact problem solving, the two-step central difference Newmark method is usually used with a set of $\alpha=0$, $\beta=1/2$.

$$\mathbf{u}^{t+\Delta t}=\mathbf{u}^{t}+\left(\mathrm{d}(\boldsymbol{u}^{t})/\mathrm{d}t\right)\Delta t+1/2\left(\mathrm{d}^2(\boldsymbol{u}^{t})/\mathrm{d}t^2\right)(\Delta t)^2 \tag{18}$$

$$\mathrm{d}(\boldsymbol{u}^{t+\Delta t})/\mathrm{d}t=\mathrm{d}(\boldsymbol{u}^{t})/\mathrm{d}t+1/2\left(\mathrm{d}^2(\boldsymbol{u}^{t})/\mathrm{d}t^2+\mathrm{d}^2(\boldsymbol{u}^{t+\Delta t})/\mathrm{d}t^2\right)\Delta t \tag{19}$$

$\boldsymbol{Q}_c^{t+\Delta t}$ can be the function of the known parameter $\boldsymbol{u}^{t+\Delta t}$, thus it can be transferred to the right side of Eq.(1) as a known parameter. Then the internal force $\boldsymbol{F}^{t+\Delta t}$ can be expressed as the below.

$$\boldsymbol{F}^{t+\Delta t}=\boldsymbol{F}^{t}+\left(\boldsymbol{K}_L^{t}+\boldsymbol{K}_{NL}^{t}\right)\boldsymbol{u}=\sum_{e}\int_{t_V}\left(\boldsymbol{B}_L^{t+\Delta t}\right)^{\mathrm{T}}\hat{\boldsymbol{\tau}}^{t+\Delta t}\mathrm{d}V \tag{20}$$

where $\left(\boldsymbol{B}_L^{t+\Delta t}\right)^{\mathrm{T}}\hat{\boldsymbol{\tau}}^{t+\Delta t}$ can also be the function of $\boldsymbol{u}^{t+\Delta t}$ and the recursion relation can be as the below.

$$\mathrm{d}^2(\boldsymbol{u}^{t+\Delta t})/\mathrm{d}t^2 = \mathbf{M}^{-1}\left(\mathbf{Q}_L^{t+\Delta t} + \mathbf{Q}_c^{t+\Delta t} - \mathbf{F}^{t+\Delta t}\right) \tag{21}$$

For the nonlinear contact problem, it is necessary to follow the search step of contact node pairs after each increment step. The calculation steps of the time integration method can be expressed as Figure 3 shows.

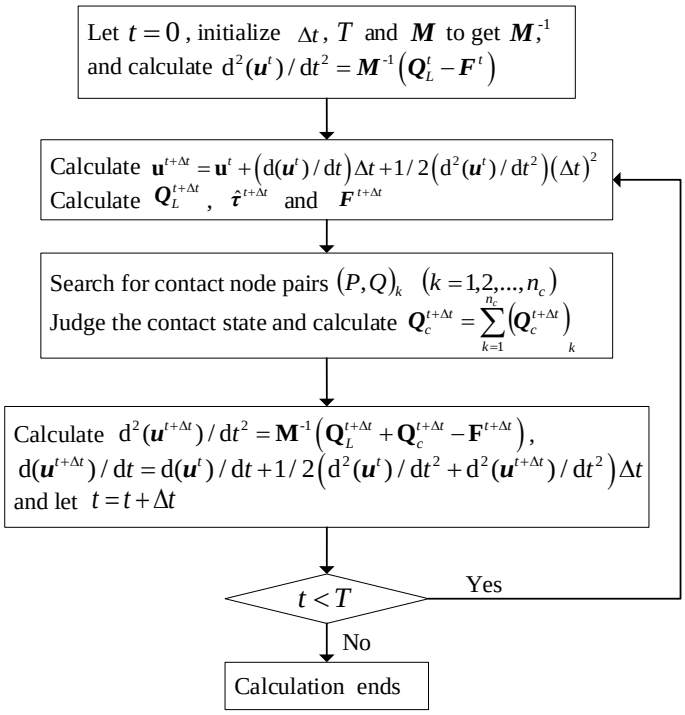

Figure 3. Solving flow of the explicit method.

3. Finite element model

The ship model and the floater model were established in Ansys Workbench first. The ship model was established according to the profile table of the actual ship design. The total length and the beam width of the ship were 102.2 m and 17.5 m, respectively. The displacement and draft of the floater were 280 t and 0.56 m. The ship drafts at the displacement of 4000 t, 4500 t, 5000 t, 5500 t and 6000 t were measured 3.28 m, 3.62 m, 3.99 m, 4.34 m, and 4.69 m (t refers to tonnage). The ship model had been meshed by the shell elements with a set of unified 20 mm wall thickness. Moreover, the element size of the ship bow and the main hull was 0.5 m. Internal plates had been meshed by a set of unified 10 mm wall thickness shell elements. The floater model could be 2 m high with a draft of 0.56 m. The element size of the floater at the contact region was 0.5 m with a unified 12 mm wall thickness. The floater model and the ship model were divided into 10,863 shell elements and 10,551 shell elements respectively, just as shown in Figure 4. To clarify grid convergence, the ship model was also meshed by the 0.2 m shell elements for comparison. The impact force results of the two different grid meshing method in Figure 5 indicate there is only a slight difference between the two curves, which clarifies

the grid convergence.

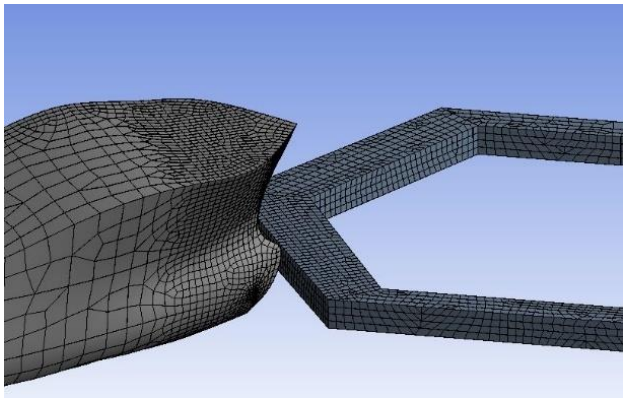

Figure 4. Finite element division of the model.

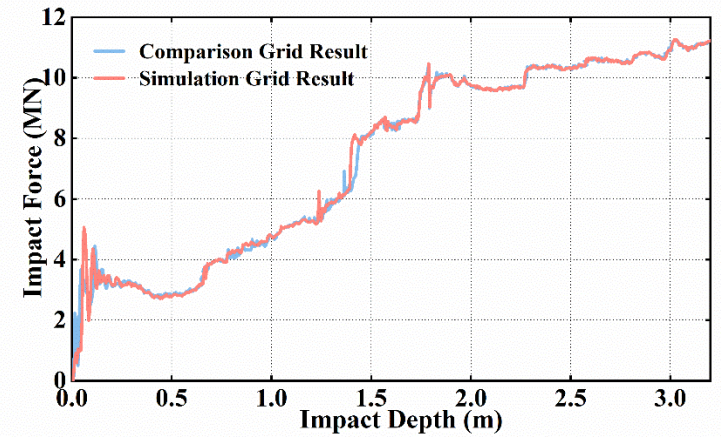

Figure 5. The result comparison between the two grid size.

The ship motion is restricted to horizontal in the local simulation, as shown in Figure 1. The floater suffers from the force of the damping cables at beam 1, 2, 3 and 4 and is accompanied by very small structural deformation at the first stage. Thus, it is reasonable to set the boundary condition above. The floater's mass is much smaller than the ship's and the contact force can only bring a minor deformation to the contact region in the initial stage, then the floater will move forward to the pier together with the ship in the later period. The local collision cannot cause great damage and the impact depth is set 3.5 m tentatively, which will be checked in 4.4.1. The automatic surface to surface has been set as the contact mode in the local simulation in which the contact node pairs can be searched for automatically and it is a kind of bilateral contact, which can convert the contact problem into the Differential-Algebraic Equations.

The materials of the ship bow and the floater selected the low carbon steel with the constitutive relationship of the bilinear hardening rule. The mass density of the colliding bodies is 7850 kg/m^3 and the Young's modulus is 207 GPa. Poisson's ratio was 0.33 and the tangent modulus was 715 MPa. The yield stress is 234 MPa and the failure strain was 0.26. The dynamic effect of the material is considered for the large deformation in the local impact and the strain rate is introduced with the Cowper Symonds strain rate model (Mirmomeni et al. 2016). Moreover, the strain limit for eroding elements in the simulation has been set to 0.22 and the element will be designated as failed and eliminated if the element strain exceeds 0.22. The static coefficient of friction, the dynamic coefficient of friction and the exponential decay coefficient have been set to 0.2, 0.1, and 0.001, respectively.

4. Collision simulation and results

4.1 Load cases

The FTBCPS can be applicable to navigable waters, and the ship can impact on the floater with

different angles. Different impact angles correspond to different penetration depths, and the impact force changes accordingly. Moreover, the impact velocity, the ship displacement and the impact position also have influence on the impact force. The impact position here means the horizontal impact position, while the vertical impact position can be affected by the ship displacement. A total 38 different load cases are conducted to study the effects of the factors mentioned above on the impact force, as shown in Table 2. Figure 6 shows the position relationships of the ship and the floater in typical load cases with different impact angles and impact positions. The elastic-plastic deformation occurs at the initial stage, and the deformation results of the ship bow and the floater in some typical load cases are shown in Figure 7.

Table 2. The load case set.

Serial number	1	2	3	4	5	6	7	8	9	10	11	12	13
Impact angle (°)	-80	-70	-60	-50	-40	-30	-20	-10	0	10	20	30	40
Ship displacement(t)	5000	5000	5000	5000	5000	5000	5000	5000	5000	5000	5000	5000	5000
Impact velocity(m/s)	5	5	5	5	5	5	5	5	5	5	5	5	5
Impact position	Centre	Centre	Centre	Centre	Centre	Centre	Centre	Centre	Centre	Centre	Centre	Centre	Centre
Serial number	14	15	16	17	18	19	20	21	22	23	24	25	26
Impact angle (°)	50	60	70	80	0	0	0	0	0	0	0	0	0
Ship displacement(t)	5000	5000	5000	5000	5000	5000	5000	5000	5000	5000	5000	5000	5000
Impact velocity(m/s)	5	5	5	5	3	3.5	4	4.5	5.5	6	6.5	7	7.5
Impact position	Centre	Centre	Centre	Centre	Centre	Centre	Centre	Centre	Centre	Centre	Centre	Centre	Centre
Serial number	27	28	29	30	31	32	33	34	35	36	37	38	
Impact angle (°)	0	0	0	0	0	0	0	0	0	0	0	0	
Ship displacement(t)	5000	5000	5000	5000	5000	5000	5000	5000	4000	4500	5500	6000	
Impact velocity(m/s)	5	5	5	5	5	5	5	5	5	5	5	5	
Impact position	Centre-4	Centre-3	Centre-2	Centre-1	Centre+1	Centre+2	Centre+3	Centre+4	Centre	Centre	Centre	Centre	

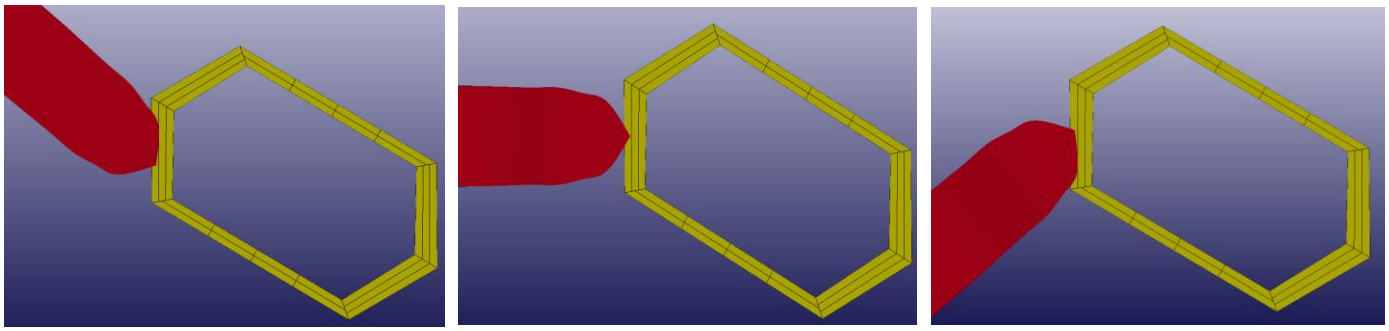

(**a**) load case 5 (**b**) load case 9 (**c**) load case 13

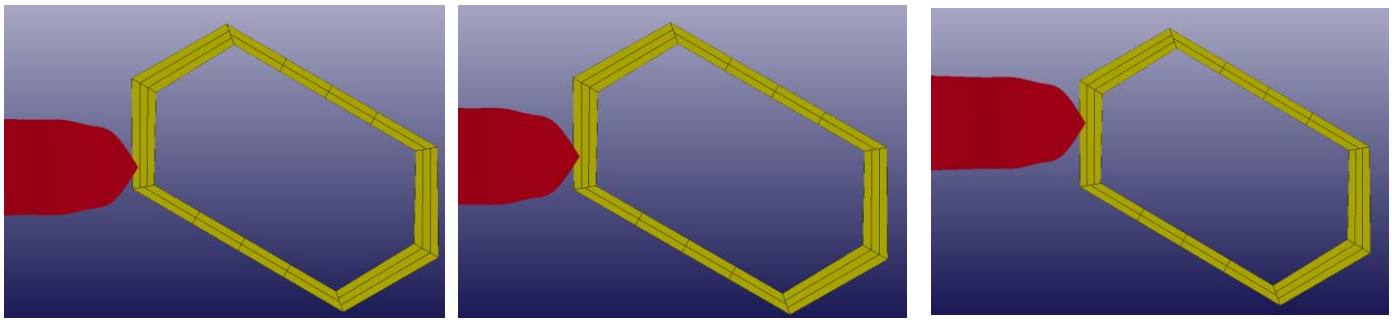

(**d**) load case 27 (**e**) load case 29 (**f**) load case 32

Figure 6. Location relationship of the objects in typical load cases.

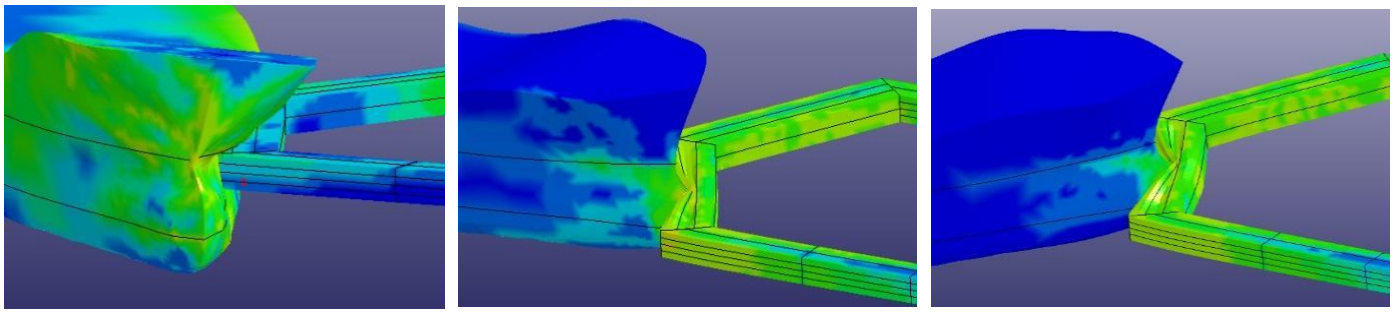

(**a**) load case 1 (**b**) load case 5 (**c**) load case 9

Figure 7. Structural deformations in typical load cases.

4.2 Comparative Analysis of the Energy and Velocity

Part of the ship kinetic energy can be converted into the internal energy in the local simulation. The energy ratio refers to the ratio of the ship kinetic energy to the total energy of the ship-floater system. The total energy includes the kinetic energy and internal energy of the ship and the floater and the system hourglass energy. The system hourglass energy is introduced to speed up the calculation process and the simulation result will be considered reliable if the hourglass energy is less than 5% of the total energy in the calculation process. The system hourglass energy in our study is less than 1%, and the simulation result can be proved effective in this respect. To some extent, the energy ratio curves can reflect the ship motion state during the impact process. It can be gained from Figure 8 that the impact angle and the impact velocity play a big role on the energy dissipation rate. Figure 8(**a**) shows that the energy dissipation rate is positively correlated with the impact angle. Figure 8(**b**) and (**c**) indicate that the influence of the impact position and the ship displacement on energy dissipation is limited. Figure 8(**d**) shows that the energy dissipation rate is negatively correlated with the impact velocity.

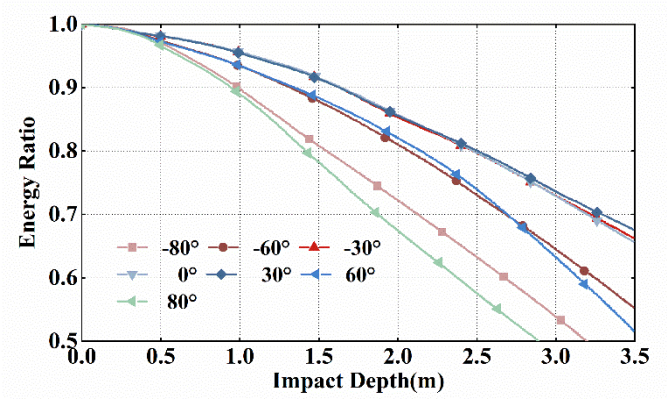

(**a**) impact angle

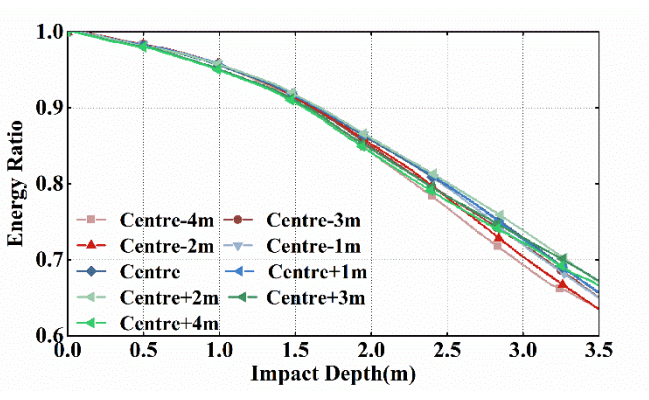

(**b**) impact position

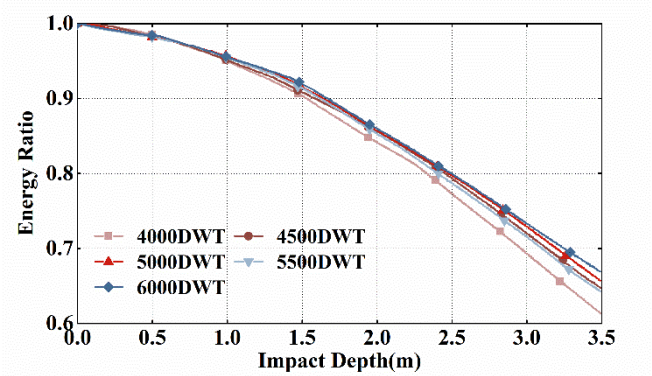

(**c**) ship displacement

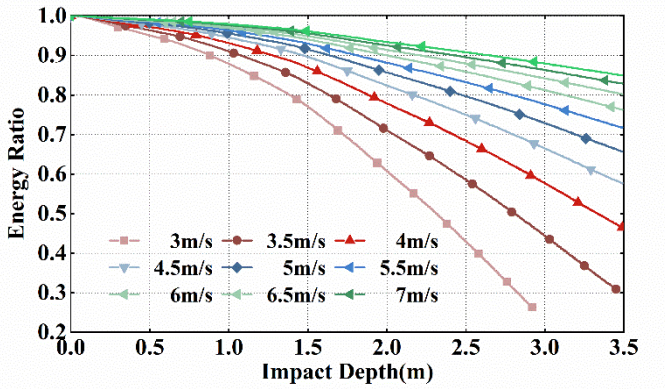

(**d**) impact velocity

Figure 8. The energy ratio comparison of different load cases.

The curves of the velocity ratio, which refers to the ratio of the ship real-time velocity to the initial velocity, can accurately reflect the ship motion state at the initial collision stage. It can be gained from Figure 9 that the comparison results of the velocity ratio and the energy ratio are roughly consistent. The impact position and the ship displacement only have a little effect on the velocity dissipation rate. It can also be gained that the velocity ratio is positively correlated with the impact angle and negatively correlated with the impact velocity, respectively. In a word, the energy ratio and the velocity ratio indicate that the impact angle and the impact velocity are the main two factors on the ship impact process, and the effects of the impact position and the ship displacement are limited.

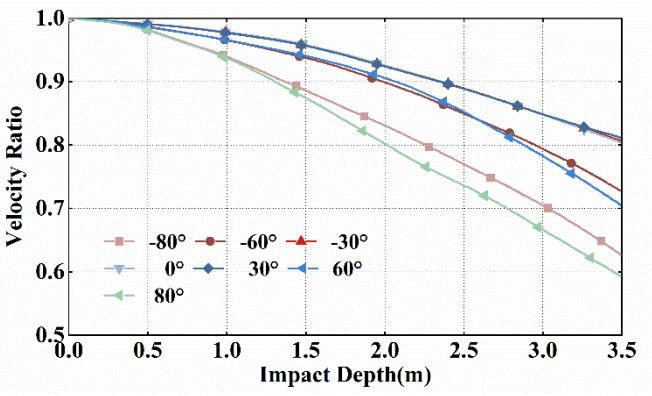

(**a**) impact angle

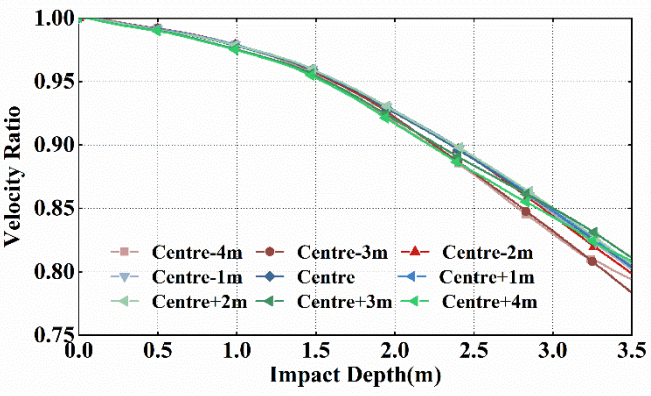

(**b**) impact position

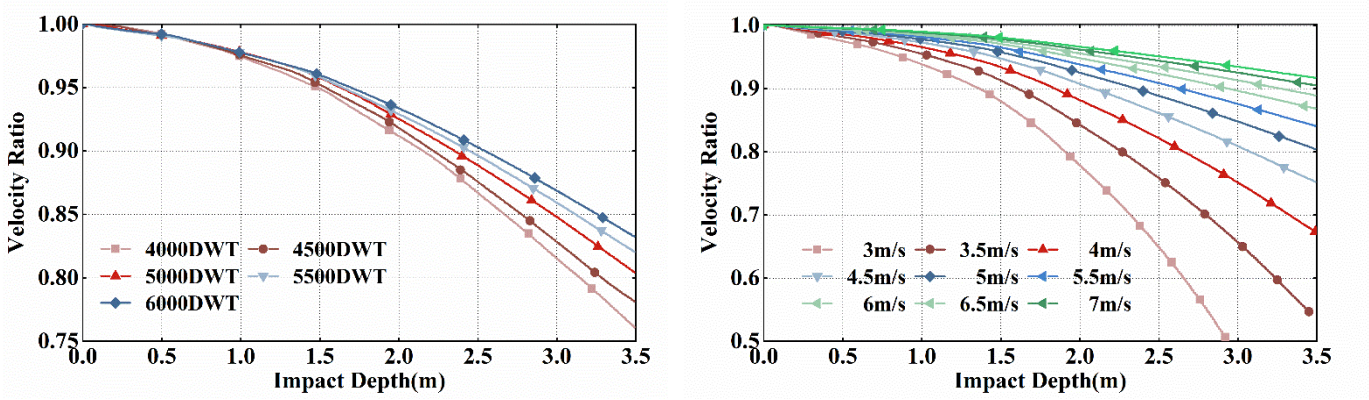

(**c**) ship displacement (**d**) impact velocity

Figure 9. The velocity ratio comparison of different load cases.

4.3 Fitting of the local impact force-depth curve

The collision process can be simplified into a node mass-spring system in the traditional method and the impact force can be gained. However, not only the impact force, but also the dynamic response of the ship and the floater will be focused on the global analysis. Thus, the whole ship will be divided into a rigid hull and a nonlinear spring system (Travanca and Hao 2015), as shown in Figure 10. The rigid hull represents the mass and the shape of the ship, and the nonlinear spring is used to replace the interaction force between the two. The stiffness value of the spring 1 can be gained from the curve fitting of the impact force-depth relationship in the local simulation. To fit in with the actual separation process, the spring 2 has been set infinite compression stiffness value and zero tension stiffness value, so that the ship can drift freely after the ship-floater separation.

Figure 11 shows the impact force-depth curves under different load cases. It can be gained from Figure 11(**a**) and (**b**) that the result curves of the load cases at an impact angle below 40° are roughly consistent, but the curves of the load cases at an impact angle over 40° show different trends. Moreover, the peak force is positively correlated with the impact angle and the reason is that a larger impact angle brings about a larger contact region and a faster energy/velocity dissipation rate. It can be gained from Figure 11(**c**), (**d**) and (**e**) that the curves of load cases with different impact positions, ship displacements and impact velocities are roughly the same and the ship displacement is relatively the most influential factor among them. The reason for it is that the ship draft and the actual contact region change with the ship displacement, and it influences the impact curve trend finally. However, the effect of the ship displacement is still limited, and it also shows the rationality of the ship added mass coefficient 0.2 in Assumption 2. In a word, the impact angle is the only and the most important factor in the ship impact process, and then the research will focus on the impact force-depth curve fitting of the load cases with different impact angles.

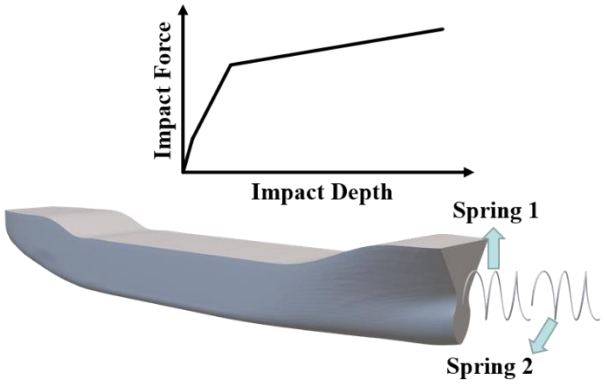

Figure 10. Rigid hull-nonlinear spring system.

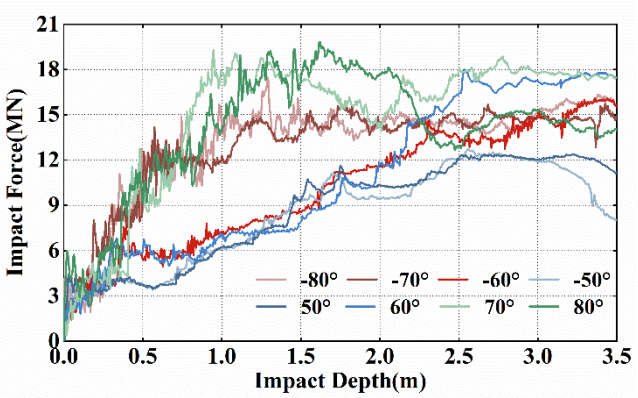

(**a**) impact angle more than 40°

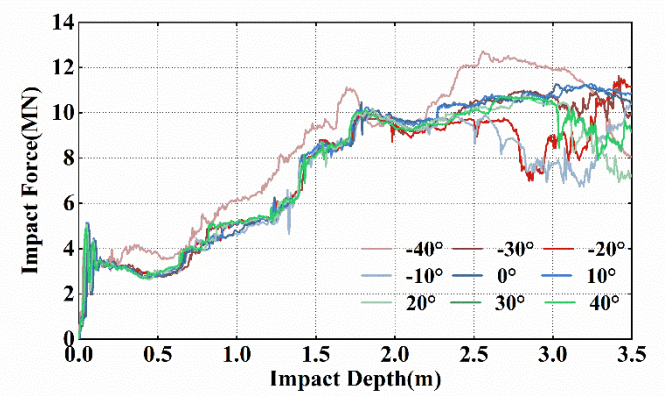

(**b**) impact angle less than 40°

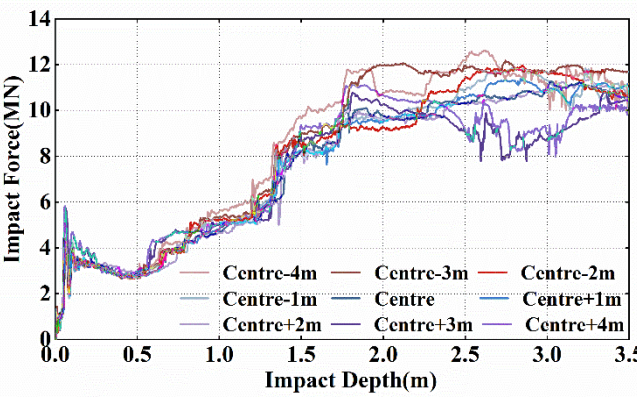

(**c**) impact position

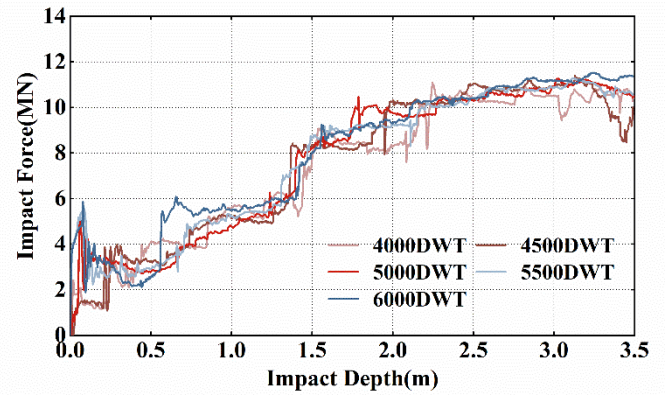

(**d**) ship displacement

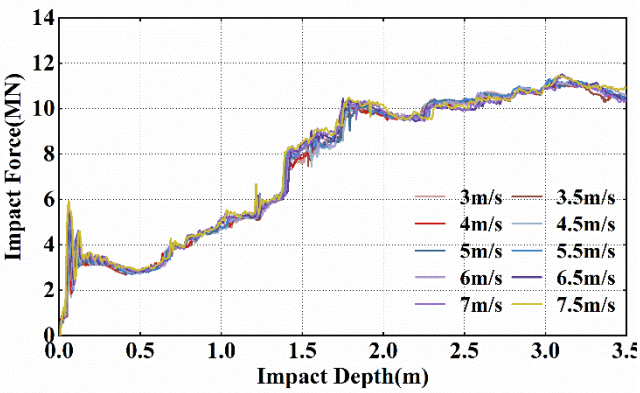

(**e**) impact velocity

Figure 11. The impact force-depth curves comparison of different load cases.

Before applied to the global analysis, the local simulation results need to be fitted into the equivalent spring stiffness values. The approach of the curve fitting taken in this paper is that some feature points are selected in the local simulation result to form the fitting curves first, and then the curves obtained will be checked. Figure 12 shows the local simulation results and the fitted stiffness values of load cases at some typical impact angles. For the deformation of the floater is not the main way to resist the ship and dissipate the ship kinetic energy in the first stage, the actual deformation of the floater will be minor. Thus, the impact depth range can meet the requirements in the global analysis, which will be verified in section 4.4.1. It is obvious that the fitted nonlinear spring stiffness values are

well matched with the local simulation results and the consistency of the two will be verified in section 4.4.3.

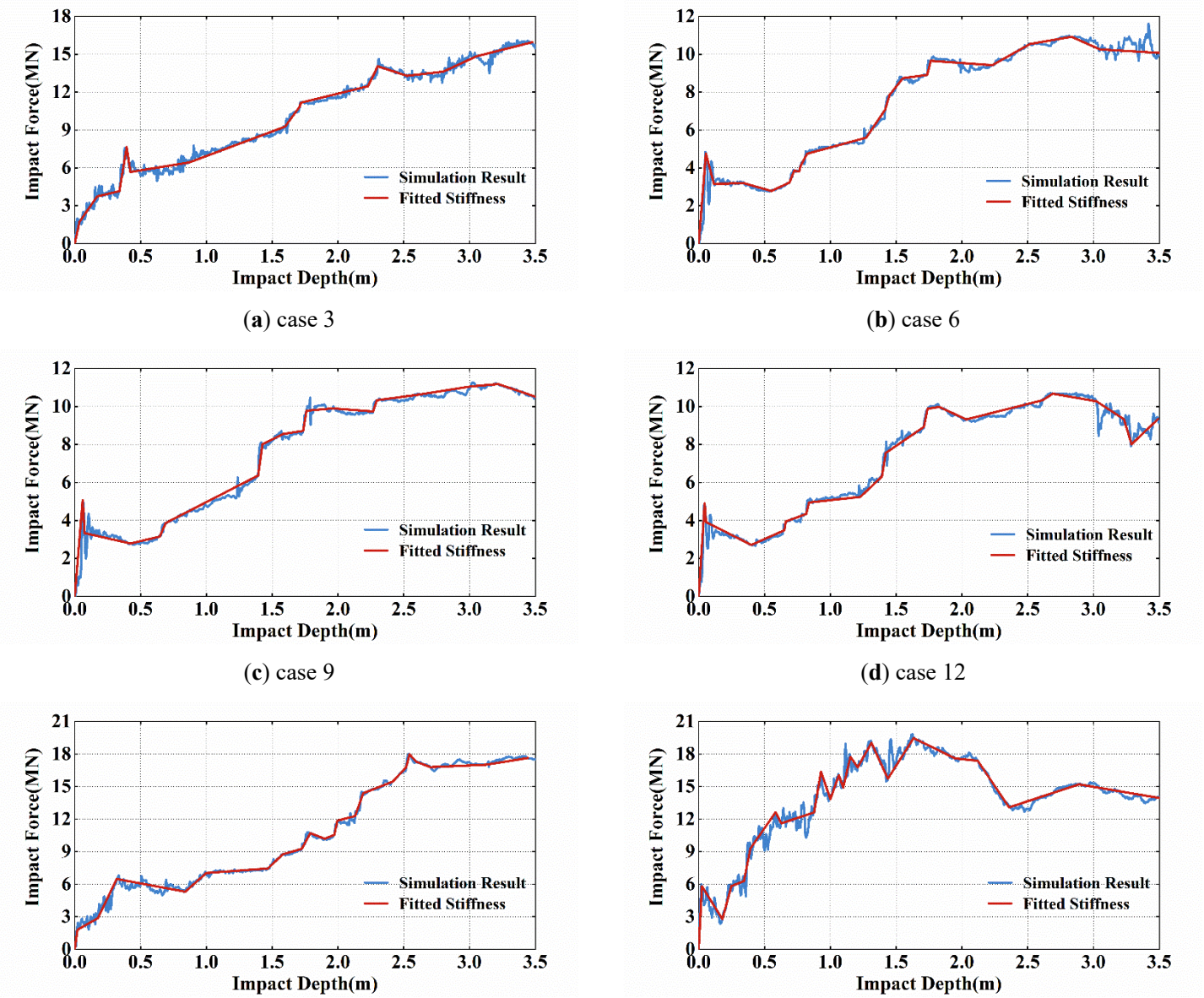

(**a**) case 3 (**b**) case 6

(**c**) case 9 (**d**) case 12

(**e**) case 15 (**f**) case 17

Figure 12. The curve fitting of different impact angle load cases.

4.4 Verification of the local simulation results

Three activities have been carried out to verify the validity of the local simulation. The first one is about the impact depth range. The value to verify is that whether the impact depth range gained in the local simulation can meet the calculation requirements in the global simulation. The second one is about the validity of the simulation results. The impact force results from a typical empirical formula will be used to test and verify the simulation results. The third one is about the consistency between the fitting stiffness values and the simulation results. The time-history curves of the impact force from

the fitted stiffness values will be compared with the curves from the original simulation data.

4.4.1 Verification of the impact depth range

The contact stiffness values have already been fitted in section 4.3 and the impact depth range needs to be tested if it can meet the requirements in the global analysis. It is equivalent to verify the impact depth 3.5 m is enough. In the global analysis, the floater starts moving from stationary and goes advance under the ship impact, at the same time, suffers from the force of damping cables. The number of damping cables in action changes with the impact process, and the number 4 is set as an assumption to verify the impact depth range. Each damping cable shares the same force-stretching distance relationship and the values of the displacement difference between the ship and the floater have been calculated at the assumption of ignoring the rotation of the floater, and the impact depth range will be accepted if the value is less than 3.5m. The values of the displacement difference under 7 typical load cases are all within 1.2 m, as shown in Figure 13, which can illustrate the impact depth range 3.5 m is enough in the global analysis.

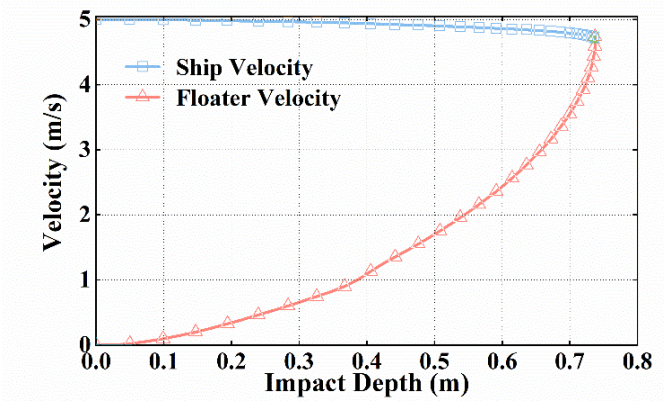

(**a**) case 3

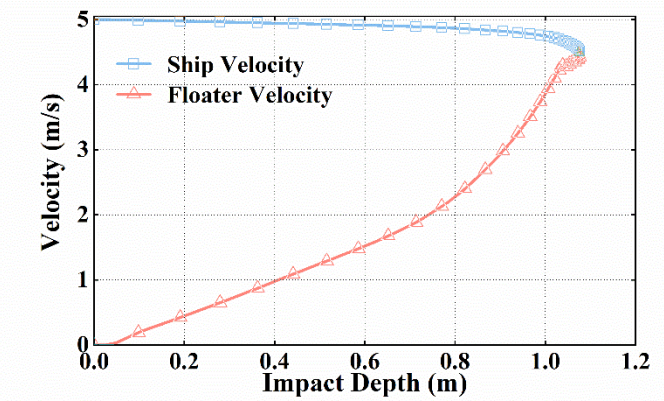

(**b**) case 6

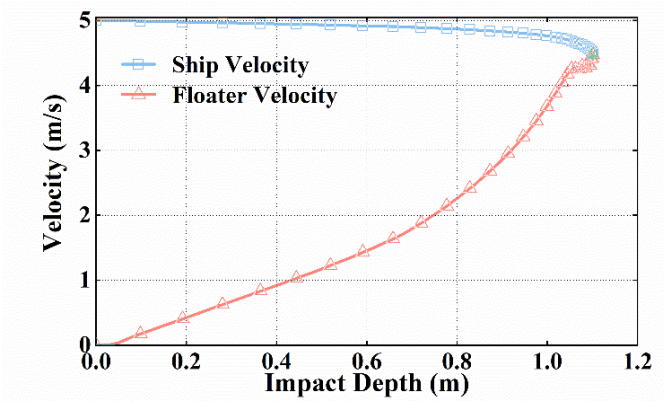

(**c**) case 9

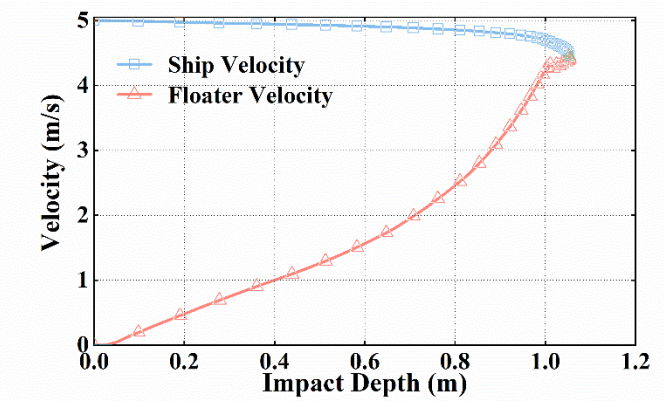

(**d**) case 12

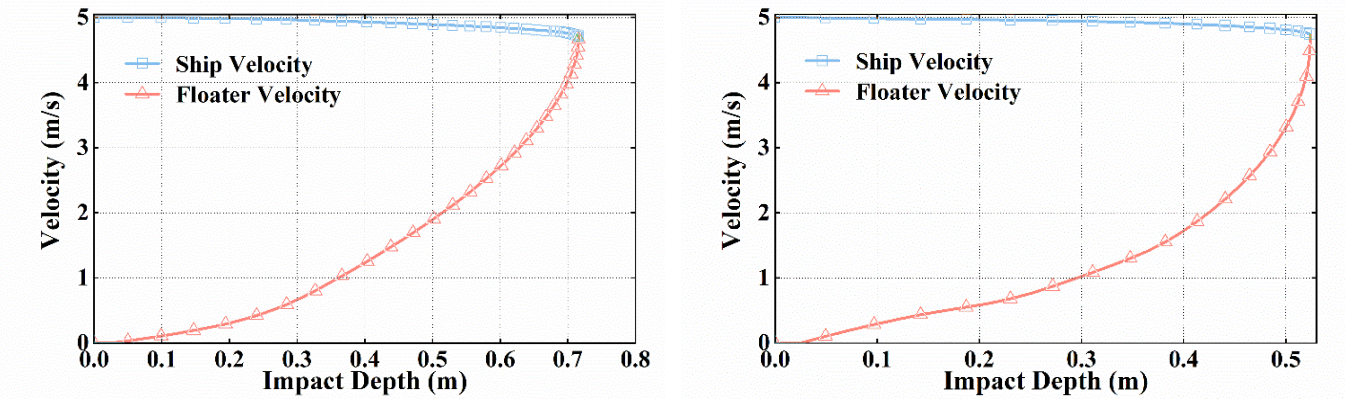

(**e**) case 15 (**f**) case 17

Figure 13. Impact depth range verification of impact angle load cases.

4.4.2 Verification of the validity of the local simulation results

The local impact process has been simulated and the impact force results are also presented in section 4.3. Then, it is reasonable to verify the validity of the local simulation process by the force results. The average impact force between the ship and the floater from the formula in 'Code for Design on Railway Bridge and Culvert' (TB 10002-2017 2017) can be used as a comparison.

$$F = \gamma \cdot v_c \sin \alpha_c \cdot \sqrt{\frac{W}{C_1 + C_2}} \tag{22}$$

where γ, in units of $\mathrm{s/m^{1/2}}$, refers to the kinetic energy reduction factor, the value of it is set 0.3 when the ship impacts on the target surface along the normal direction and set 0.2 in the other load cases. v_c refers to the ship velocity. α_c refers to the angle between the direction of the ship moving on and the tangent line of the target surface. C_1 refers to the elastic deformation coefficient of the ship and C_2 refers to it of the floater. The sum of C_1 and C_2 is set 0.0005 by default. The impact force F and the ship weight W are both in units of kN.

The impact process is extremely complex, and the impact force may be related to a series of influencing factors, e.g., the ship shape, the ship material, the impact angle, and the impact location. Thus, the results in Eq.(22) can only be used as a reference to roughly examine the simulation result. The peak value of the impact force obtained in Eq.(22) is 15 MN when 5000 t ship impacts on the floater along the normal direction at a velocity of 5 m/s, which roughly matches the result of the maximum impact force 11.8 MN in Figure 13(**i**). That means the simulation result can be verified by the empirical formula.

4.4.3 Verification of the consistency of the fitted stiffness value

To verify the consistency of the fitted stiffness values in section 4.3, the correlation coefficient method (Sheng et al. 2008) is introduced here and the correlation coefficient ρ_{12} will be used to calculate the correlation of the simulation result curve and the fitted stiffness curve.

$$\rho_{12}=\frac{\frac{1}{n}\sum_{i=1}^{n}y_{1i}\cdot y_{2i}-\frac{1}{n^2}\sum_{i=1}^{n}y_{1i}\cdot\sum_{i=1}^{n}y_{2i}}{\frac{1}{n-1}\sqrt{\sum_{i=1}^{n}\left(y_{1i}-\frac{1}{n}\sum_{i=1}^{n}y_{1i}\right)^2\cdot\sum_{i=1}^{n}\left(y_{2i}-\frac{1}{n}\sum_{i=1}^{n}y_{2i}\right)^2}} \tag{23}$$

where the closer the correlation coefficient ρ_{12} gets to 1, the higher the positive correlation of the two curves will be.

The results of the correlation coefficient in Table 3 show that the curves are of good consistency and mean that the fitted stiffness values can bring the similar effects to the local simulation results.

Table 3. The correlation coefficient of the fitted stiffness values.

Serial number	1	2	3	4	5	6	7	8	9
Correlation coefficient	0.975	0.979	0.996	0.988	0.995	0.992	0.988	0.987	0.992
Serial number	10	11	12	13	14	15	16	17	
Correlation coefficient	0.992	0.990	0.988	0.995	0.996	0.997	0.992	0.988	

5. Conclusions

The calculation method of the contact stiffness values is proposed, and an impact example has been given in this method. The initial impact responses under the various load cases are studied and the results have been verified.

(1) The dissipation processes of the energy and the velocity in the load cases with diverse factors are investigated. The impact angle and impact velocity are the main factors as far as the energy/velocity dissipation rate is concerned.

(2) The relationship of the impact force and the impact depth in the load cases with distinct factors is considered, and the impact angle is found to be the only significant one of them. The impact force-depth curves at different impact angles are fitted and the contact stiffness values in each impact depth intervals are given, which is meaningful to the global analysis.

(3) The contents of validation include the impact depth range, the validity of the local simulation results and the consistency of the fitted stiffness values. The results indicate that the fitted stiffness values are useful and lay a great foundation for the global analysis on the FTBCPS.

References

Chen L, Lu H and Li H (2019) Dimension-by-dimension enhanced cuckoo search algorithm for global optimization. *Soft Computing* 23(21), 11297-11312.

Consolazio GR, Davidson MT and Cowan D R (2009) Barge bow force-deformation relationships for barge-bridge collision analysis. *Transportation Research Record* 2131: 3-14.

Consolazio GR and Davidson MT (2008) Simplified dynamic analysis of barge collision for bridge design.

Transportation Research Record 2050: 13-25.

Fan W, Zhang ZW, Huang X and Sun WB (2020) A simplified method to efficiently design steel fenders subjected to vessel head-on collisions. *Marine Structures* 74: 102840.

Gholipour G, Zhang CW and Kang WH (2020) Nonlinear numerical analysis and progressive damage assessment of a cable-stayed bridge pier subjected to ship collision. *Marine Structures*, 69: 102662.

Gholipour G, Zhang CW, Kang WH and Mousavi AA (2019) Reliability analysis of girder bridge piers subjected to barge collisions. *Structure and Infrastructure Engineering* 15(9): 1200-1220.

Guo X, Zhang C and Chen ZQ (2020a) Nonlinear dynamic response and assessment of bridges under barge impact with scour depth effects. *Journal of Performance of Constructed Facilities* 34(4): 04020058.

Guo X, Zhang C and Chen ZQ (2020b) Dynamic performance and damage evaluation of a scoured double-pylon cable-stayed bridge under ship impact. *Engineering Structures* 216: 110772.

Jiang H and Chorzepa MG (2016) Case Study: Evaluation of a Floating Steel Fender System for Bridge Pier Protection against Vessel Collision. *Journal of Bridge Engineering* 21(11): 05016008.

Kameshwar S and Padgett JE (2018) Response and fragility assessment of bridge columns subjected to barge-bridge collision and scour. *Engineering Structures* 168: 308-319.

Li WK and Mao J (2014) Symmetric penalty function method used for the analysis of contact of round link chain transmission process. *Journal of Liaoning Technical University (Natural Science)* 33(11): 1530-1533.

Manohar T, Suribabu CR and Salaimanimagudam MP (2020) A novel steel-PAFRC composite fender for bridge pier protection under low velocity vessel impacts. *Structures* 26: 765-777.

Minorsky VU (1958) An analysis of ship collisions with reference to protection of nuclear power plants. *Journal of Ship Research* 3(2): 1-4.

Mirmomeni M, Heidarpour A, Zhao XL, et al. (2017) Size-dependency of concrete-filled steel tubes subject to impact loading. *International Journal of Impact Engineering* 100(2): 90-101.

Moe OH, Sha Y and Veie J (2017a) Analysis of tether anchored floating suspension bridge subjected to large ship collisions. *Procedia Engineering* 199: 2488-2493.

Moe OH, Aas JK and Amdahl J (2017b) Analysis of tether anchored floating suspension bridge subjected to extreme environmental loads. *Procedia Engineering* 199: 3033-3038.

Petersen MJ (1982) Dynamics of ship collisions. *Ocean Engineering* 9(4): 295-329.

Sha YY and Amdahl J (2019a) Numerical investigations of a prestressed pontoon wall subjected to ship collision loads. *Ocean Engineering* 172: 234-244.

Sha YY, Amdahl J and Liu K (2019b) Design of steel bridge girders against ship forecastle collisions. *Engineering Structures* 196: 1-14.

Sha YY, Amdahl J and Dorum C (2017) Dynamic responses of a floating bridge subjected to ship collision load on bridge girders. *Procedia Engineering* 199: 2506-2513.

Sheng Z, Xie SQ and Pan CY (2008) *Probability theory and mathematical statistics*. Beijing: Higher Education Press.

TB 10002-2017 (2017) *Code for design on railway bridge and culvert*.

Travanca J and Hao H (2015) Energy dissipation in high-energy ship-offshore jacket platform collisions. *Marine Structures* 40: 1-37.

Wang W, Morgenthal G and Kraus M (2020) Numerical evaluation of a novel crashworthy device for pier protection from barge impact. *Engineering Structures* 212: 110535.

Wang W and Morgenthal G (2018a) Reliability analyses of RC bridge piers subjected to barge impact using efficient models. *Engineering Structures* 166: 485-495.

Wang W and Morgenthal G (2018b) Novel Crashworthy Device for Pier Protection from Barge Impact. *Advances in Civil Engineering* 2018: 9385643.

Wang W and Morgenthal G (2017) Dynamic analyses of square RC pier column subjected to barge impact using efficient models. *Engineering Structures* 151: 20-32.

Wang XC (2003) *Finite element method*. Beijing: Tsinghua University Press.

Wang ZL, Jiang ZY and Gu YN. An added water mass model for numerical simulation of ship/ship collision. *Explosion and Shock Waves* 22(4): 321-326.

Zhu L, Liu W and Fang H (2018) Design and simulation of innovative foam-filled Lattice Composite Bumper System for bridge protection in ship collisions. *Composites Part B-Engineering* 157: 24-35.